

Convective Building of a Pycnocline: A Two-Dimensional Nonhydrostatic Numerical Model

DAVID W. PIERCE* AND PETER B. RHINES

School of Oceanography, University of Washington, Seattle, Washington

(Manuscript received 1 December 1995, in final form 24 September 1996)

ABSTRACT

The convective building of a pycnocline is examined using a two-dimensional nonhydrostatic numerical model forced by a balanced salinity dipole (source and sink). Although the forcing fields are steady, the model develops oscillations that renew the model's analog of "deep waters" only intermittently. The oscillation cycle consists of a freshwater layer that advects along the surface, capping off the water column under the dense source and preventing sinking; after a time, continuing densification forms a plume that breaks through the salinity barrier and convects beneath the dense source, ventilating the deep water. Increasing the viscosity reduces but does not eliminate this cycle. When the hydrostatic assumption is added, the model evolves systematically different salinity distributions than the nonhydrostatic model due to the isolation of part of the tank by a persistent convective column. The deep flow is also different in this case because of differences between the entrainment/detrainment profile of a hydrostatic plume and one modeled explicitly. The model evolves a characteristically skewed distribution of densities that is similar to the distribution of temperature in the World Ocean. Rotation increases the range of this distribution due to the inhibition of meridional flow.

1. Introduction

The thermohaline circulation of the oceans is an important example of buoyancy-driven flow in a stratified fluid. In such flows convection helps create the background stratification in the fluid and then is modified by the stratification. Despite the intimate association between convection and stratification there has been little work examining the two in a coupled system.

Numerical work examining convection has often assumed either a neutral or initial background stratification that is stipulated independently of the convection (e.g., Jones and Marshall 1993). This is perfectly justified when considering individual convective plumes that by themselves have little effect on the background stratification. Here, however, we are interested in the long timescales over which the convection *determines* the background stratification.

To a good approximation the thermohaline circulation is driven not by a net buoyancy flux but by a spatial separation of equal but opposite buoyancy fluxes with a net of zero. Much laboratory work examining con-

vection has been driven by a net buoyancy flux; when the laboratory fluid becomes too light or too dense or the buoyancy gradients vanish, the experiment is considered "over." Here we are interested in the geophysically relevant situation of *no* net buoyancy flux and again the long-time behavior of the system is the point of interest.

We examine the convective building process using a two-dimensional nonhydrostatic numerical model configured to be similar to the laboratory experiments of Pierce and Rhines (1996; PR1 hereafter). Our objective is to examine the energy evolution and population distributions of density in the system to the extent possible, aspects of the laboratory experiments of PR1 that are difficult to measure without disturbing the flow, and to compare these distributions to those observed in the earth's oceans. Additionally, contrasting the numerical results to the known laboratory results will indicate areas in which the numerical model is deficient; we then attempt to extrapolate this understanding to large-scale models of the earth's thermohaline circulation.

This work is arranged as follows. Section 2 gives an overview of the model's derivation (details are given in the appendix). Section 3 gives results for the various test cases: the control run; a run with rudimentary effects of rotation included; the effect of making the hydrostatic approximation; and the effect of high diffusion. Section 4 discusses the results, and section 5 presents the conclusions.

*Current affiliation: Scripps Institution of Oceanography, University of California, San Diego, San Diego, California.

Corresponding author address: Dr. David W. Pierce, Climate Research Division, 0224, Scripps Institute of Oceanography, La Jolla, CA 92093-0224.
E-mail: dpierce@uscd.edu

2. Model formulation

It is worth carefully considering the correspondence between the “small scale” numerical model described here, which is intended to model a 1-m-long laboratory experiment, and “large scale” two-dimensional numerical models intended to model the entire earth’s global thermohaline circulation, such as those used by Marotzke and Willebrand (1991), Stocker et al. (1992), and Winton and Sarachik (1993). Comparing the governing equations of the model used here (presented below) to those of the large-scale models, it is evident that they are similar except in two respects: 1) the small-scale model is nonhydrostatic and so includes a prognostic equation for the vertical velocity; the large-scale models assume vertical hydrostatic balance. 2) Large-scale models use large values for viscosity and diffusivity (“eddy diffusivities”), while the values used here are close to molecular values. Based on this correspondence between the large- and small-scale models we expect that some of the observations of the small-scale model described here will be applicable to the 2D large-scale models also and, with proper interpretation, to the earth’s thermohaline circulation.

This comparison can be made more quantitative by examining the relevant nondimensional parameters of the modeled flow: the Reynolds number, the aspect ratio, and (when rotating) the Rossby number. In comparing these parameters for the flow modeled here to those of the ocean, we use so-called eddy values for oceanic viscosity and diffusivity rather than molecular values. In regions or situations where oceanic mixing processes are not well characterized by such an approach, this comparison will not be valid; this indicates a fundamental limitation of the numerical model used here that must be kept in mind.

The Reynolds number (Re) is given by UL/ν , where U is a characteristic velocity, L the length scale, and ν the viscosity. Using eddy viscosities, appropriate numbers for a large-scale model of the earth’s thermohaline circulation might be $U \sim 0.1 \text{ m s}^{-1}$, $L \sim 150^\circ$ latitude, and $\nu \sim 1 \times 10^3 \text{ m}^2 \text{ s}^{-1}$, giving $Re \sim 1.5 \times 10^3$. For the model developed here $U \sim 3 \times 10^{-3} \text{ m s}^{-1}$, $L \sim 0.75 \text{ m}$, and $\nu = 1 \times 10^{-6} \text{ m}^2 \text{ s}^{-1}$, giving $Re \sim 2.5 \times 10^3$, reasonably close to the value for a large-scale model.

The difference is greater for the aspect ratio $\delta = L/D$ (where D is the depth); for the thermohaline circulation $D \sim 5 \times 10^3 \text{ m}$, giving $\delta \sim 3 \times 10^{-4}$. For the small-scale model $D = 0.16 \text{ m}$, giving $\delta \sim 0.2$. The extreme smallness of δ (and therefore the largely horizontal nature of motion in the earth’s oceans) is the primary justification for the hydrostatic assumption being made in large-scale models of the earth’s thermohaline circulation. Nevertheless, this assumption is poor in convective regions, which are an important point of interest here. This issue will be explored in detail by examining the behavior of the model both with and without the hydrostatic assumption.

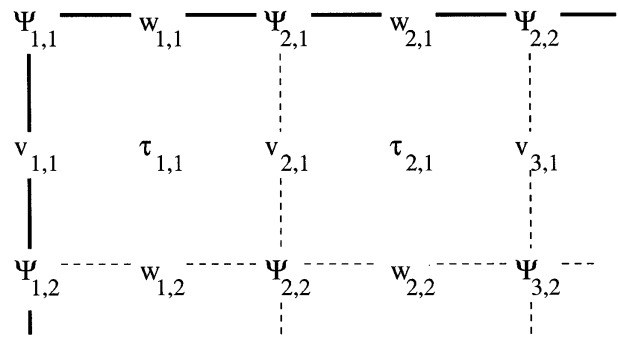


FIG. 1. Grid arrangement for the model. Here Ψ indicates streamfunction points; v , horizontal velocity points; w , vertical velocity; and τ , tracers. Heavy lines indicate a solid boundary.

Details of derivation of the model’s equations are shown in the appendix; this section gives an overview of the process. The model is two-dimensional and is assumed to be Boussinesq and incompressible but not hydrostatic; such an “anaelastic” system was first studied in this context by Ogura and Phillips (1962).

A two-dimensional model in the (Y, Z) plane is formed by taking the horizontal average of the momentum equations in the X direction. A two-dimensional model with fine resolution is used in preference to a three-dimensional model with coarser resolution so that small (close to molecular) values of diffusivity can be used without the results being overwhelmed by numerical diffusivity. However, this choice removes the role of flow variations in the X direction, which has some consequences on the flow that are pointed out in the relevant sections below.

A streamfunction Ψ can be defined by the relations $\Psi_z = -V$, $\Psi_y = W$ where V and W are the velocities in the Y and Z directions, respectively, averaged in the X direction. Taking the curl of the momentum equations and making use of the horizontal vorticity $\zeta = W_y - V_z \equiv \nabla^2 \Psi$ yields

$$\frac{\partial}{\partial t} \nabla^2 \Psi + \mathbf{J}(\Psi, \zeta) - (fU)_z = -\frac{g}{\rho_o} \rho'_y + \mu \nabla^2 \zeta, \quad (1)$$

where f is the Coriolis parameter, U is the velocity in the X direction averaged in that direction, g is the gravitational acceleration, ρ_o is a characteristic density, ρ' is the perturbation density, and ν is the viscosity. Examining the terms from left to right, this equation shows that the horizontal vorticity can change due to the advection of the vorticity by the flow field, by a “tipping” of water columns in the presence of rotation, by an imposed density torque, or by viscous diffusion.

The model numerically solves Eq. (1) along with a tracer conservation equation (salinity is used here) on a staggered grid using a leapfrog time scheme. The grid is shown in Fig. 1. A half time step backward was performed every 20 leapfrog steps followed by a forward step to prevent time level splitting. An outline of

the sequence used to step Ψ forward in time is shown in Fig. 2.

The tracer advection scheme is an adaptation of the piecewise parabolic method (Colella and Woodward 1984) to a two-dimensional, flux conservative form for use on a staggered grid. This advection scheme was chosen because it is positive definite but has less numerical diffusion than other such schemes, such as Smolarkiewicz (1983). A scheme with low numerical diffusion is important for a model of convection because it allows sharp gradients to form; the sharp gradients are necessary to develop Richardson number instabilities that play a role in entraining fluid into the convecting element.

Energy equations

Equations for the evolution of kinetic (\mathcal{K}) and potential (\mathcal{P}) energy integrated over the volume of the model (derived in the appendix) can be written as

$$\frac{D\mathcal{P}}{Dt} = \int \left(\underbrace{Wg\rho'}_{\text{CONV}} - \underbrace{2\kappa g\rho_z}_{\text{CM}} + \underbrace{Q\Phi}_{\text{SRC}} \right) dV \quad (2)$$

$$\frac{D\mathcal{K}}{Dt} = \int \left(\underbrace{-Wg\rho'}_{\text{CONV}} - \underbrace{\rho_o\epsilon}_{\text{DISS}} + \underbrace{P\nabla\cdot\tilde{U}}_{\text{PW}} \right) dV, \quad (3)$$

where κ is the vertical diffusivity, Q is a source or sink of potential energy imposed at geopotential Φ (i.e., surface cooling or heating), ϵ is the dissipation (defined in the appendix), P is the pressure, and \tilde{U} is the full three-dimensional velocity field. The ‘‘CONV’’ term represents the conversion between potential and kinetic energy. A fluid parcel heavier than other parcels on the same geopotential ($\rho' > 0$) will tend to sink, generating a negative vertical velocity; thus, the $Wg\rho'$ term will be less than zero, increasing the kinetic energy and decreasing the potential energy by the same amount. The center of mass term ‘‘CM’’ represents the change in potential energy due to vertical movement of the center of mass. For a generally stable system $\rho_z < 0$ and diffusion will tend to raise the center of mass of the system, increasing the potential energy. ‘‘SRC’’ represents sources or sinks of potential energy (surface cooling or heating, respectively). ‘‘DISS’’ represents dissipation. ‘‘PW’’ represents pressure work and is identically zero here because the fluid is assumed incompressible. It is shown here for reasons that will be given in section 3.

3. Results

The domain consisted of 300 points in the horizontal and 64 points in the vertical, with a grid spacing of 2.5×10^{-3} m for a total domain 0.75 m long by 0.16 m tall. The viscosity was set to 1×10^{-6} m² s⁻¹ and the diffusivity to 0.5×10^{-6} m² s⁻¹. This value of diffusivity is more appropriate for temperature (though still larger

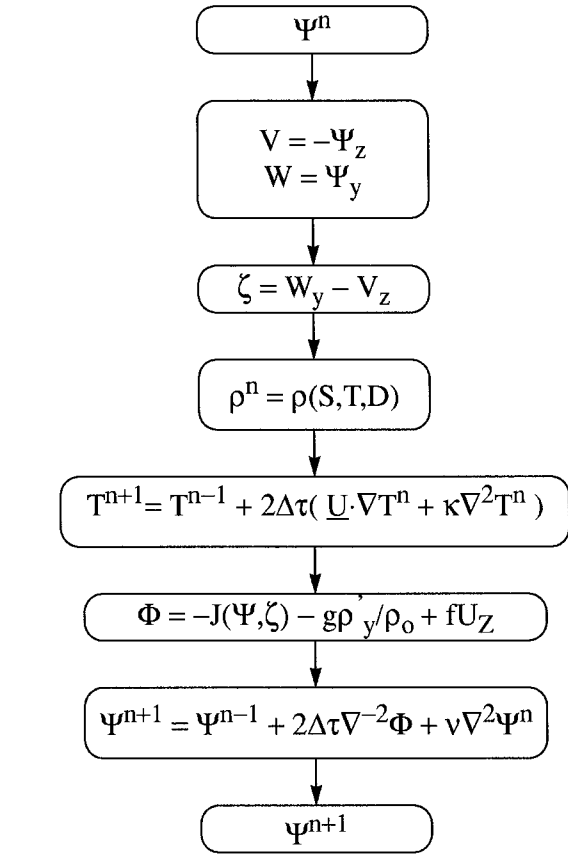


FIG. 2. Outline of the time-marching procedure. Superscripts indicate time levels; subscripts indicate derivatives.

than the molecular value) than for salinity; despite this, salinity is used here for more direct comparison with PR1. The explicit value for diffusivity was not set any lower because tests showed that numerical diffusion imposed a practical lower limit to the explicit diffusivity. Therefore, setting the explicit diffusivity lower, while possible, would have been misleading. Note that there is only a single active component to the equation of state.

a. Control run

Forcing for the control run was similar in configuration to that used in PR1. A dipole of buoyancy sources forced the model, each source having a buoyancy flux of 1.2×10^{-4} m³ s⁻³. Note that since the model is reentrant in the X direction, the source is effectively a line source of buoyancy.

The buoyancy source and sink were accomplished by directly changing the salinity values in the top layer of the model. This differs from PR1, where the forcing was produced by pumping in small volumes of fluids with known salinities and removing the same volume at an equal rate.

Figure 3 shows the early evolution of the model’s

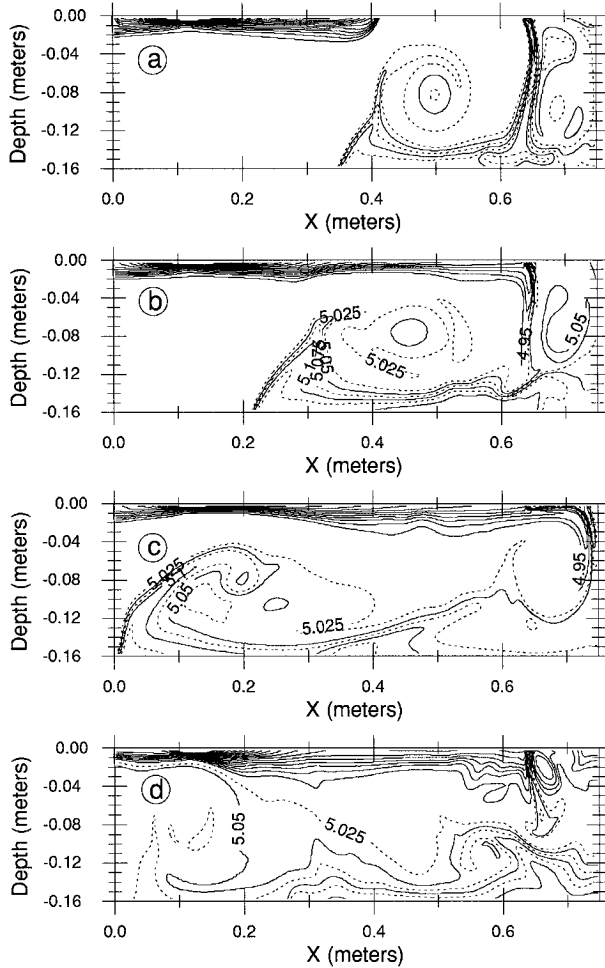


FIG. 3. Contours of salinity (percent) as a function of depth and time for the control case. For this and the following figures, the contour interval is 0.05%, with extra contours (dashed) inserted between, at multiples of 0.025%, for values greater than 5%: $T =$ (a) 2.0 min; (b) 2.8 min; (c) 3.9 min; (d) 9.6 min.

salinity field. The surface dense source is situated at the right-hand side of the tank at approximately $X = 0.64$ m, while the surface fresh source is at $X = 0.12$ m. At $T = 2.0$ min (panel a) the freshwater can be seen propagating along the surface of the tank in a bulbous-nosed

gravity current, while the salty water from the dense source is propagating along the bottom in the opposite direction. At this point, there has been no interaction between the dense and light sources, and the velocities in the interior of the tank are evolving as if the light source were not present.

The situation after 2.8 min is shown in panel b. At this point the buoyant water from the freshening source has reached the location of the dense plume. The light fluid has been drawn into the descending plume and injected into the center of the tank. This freshwater then tries to rise and by $T = 3.9$ min (panel c) this buoyant, injected water has formed a rising eddy under the dense source that sweeps the descending plume against the tank wall.

Not until $T = 9.6$ min (panel d) does this eddy dissipate, allowing a plume to reform directly beneath the dense source. The salinity of the reformed plume is less than that of the original plume, however, since it must now penetrate through the fresh upper layer. As a result, the plume penetrates only to intermediate depths.

The salinity field averaged for 10 min starting at 35 minutes is shown in Fig. 4. The model has built a deep salinity gradient by this point, increasing from 4.95% near the base of the sharp halocline to 5.15% at the bottom. In this averaged picture a persistent “chimney” appears directly beneath under the dense source, which is frequently the site of dense sinking. There is a slight bowing up of the isohalines underneath the fresh source where water lightened by diffusion tends to rise. It is interesting to note that in this averaged picture there is no indication that the deep water is ventilated—that is, the interior isohalines extend from the left wall of the tank to the right, isolating the bottom water.

The streamfunction averaged over a 10-min interval starting at 35 minutes is shown in Fig. 5. There is a strong surface-trapped circulation feeding entrainment into the dense source; on average, fluid from the dense source sinks no more than halfway through the tank before detraining from the plume and recirculating into the surface waters. There is a weak remnant of circulation that ventilates the deep waters in the tank along with some evidence of local recirculation in the deep water.

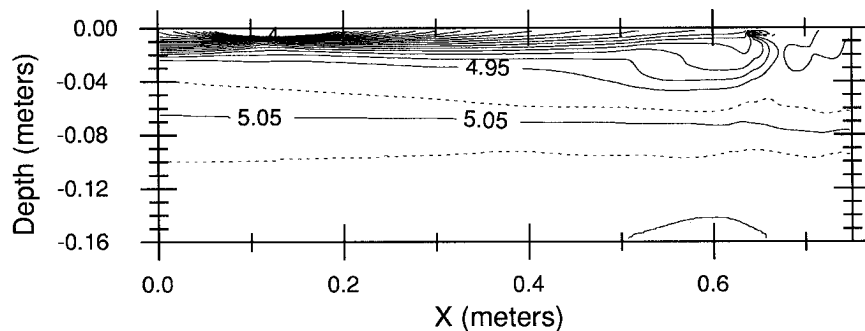


FIG. 4. The average salinity field for the control case after 35 min.

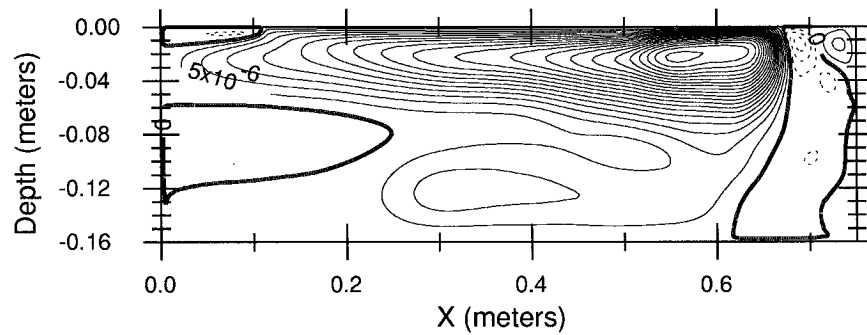


FIG. 5. The average streamfunction for the control case after 35 min.

Examination of the fields as a function of time shows that the circulation is actually proceeding through a repetitive cycle of motions illustrated using the salinity field in Fig. 6. The cycle begins with a plume sinking directly underneath the dense source and a fresh layer extending across about half the width of the tank (panel a). The fresh surface layer propagates along the top of the tank, sweeping the dense plume to the end wall, and

detaching a segment of dense plume water that descends, isolated, into the interior of the tank (panel b). The dense plume continues to sink along the end wall for about 30 seconds (panel c), but then the dense water accumulating under the salty source punches through the surface stratification and forms a new dense plume (panel d). The process then starts over again. A complete cycle takes approximately 3½ minutes.

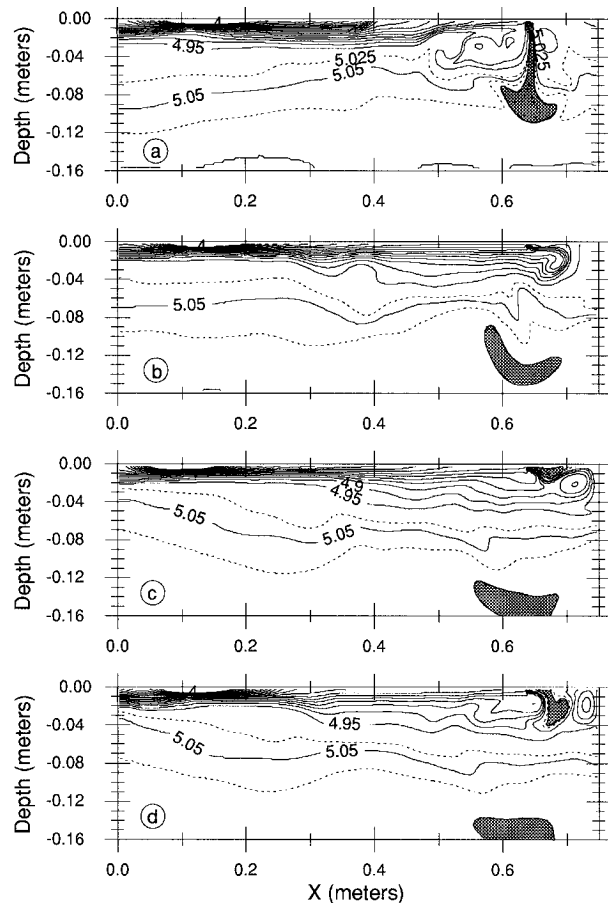


FIG. 6. Control case, illustrating the repetitive cycle by which the tank's deep fluid is renewed. Fluid of salinity greater than 5.1% is shaded.

It is interesting to observe that a bit of dense water (the shaded region in Fig. 6) reaches the bottom of the tank via this process. Thus, the model's analog of "deep water" renewal is occurring intermittently through episodic sinking events terminated by the periodic infusion of freshwater despite the fact that the forcing is steady. There are hints of this process in the average salinity field (Fig. 4) and average streamfunction field (Fig. 5). In the average salinity field, a region of high salinity can be seen under the dense source at about $X = 0.6$ m, seemingly cut off from any possible source. In the average streamfunction field, a small amount of flow into the deep water underneath the dense source can be seen. Also, in the deep waters under the dense source, the average flow crosses the average isohalines; the model is not very diffusive, so it is not possible for slow vertical flow crossing isohalines to densify by diffusion along the way. Instead, the deep flow seen in the average streamfunction field is intermittent in nature.

In order to judge how water parcels sink, the tank was seeded with 100 floats released after 40 minutes. Figure 7 is a "spaghetti plot" showing every third float track. There are two distinct sinking regions: one directly underneath the dense source and one adjacent to the right-hand wall. This is not surprising considering the cycle that the fields go through, but it is nevertheless interesting to note that the existence of *two* sinking regions is not immediately discernible from the average streamfunction field (Fig. 5). The majority of floats that sink in one of the dense plumes detrain from the sinking region at a fairly shallow depth, recirculate to the surface, and are reinjected into the interior of the tank.

Of the 100 floats released into the model, 13 descended in the dense plume directly under the source (the "left" plume), 25 descended in the plume along the

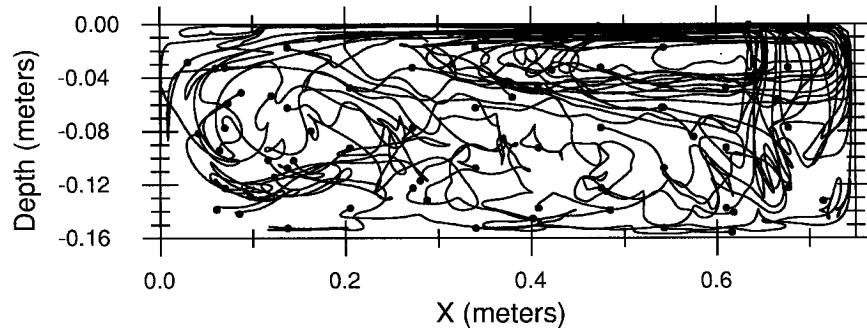


FIG. 7. Tracks of 32 floats added to the control run.

right-hand wall (the “right” plume), and 12 descended in both plumes at various times. Tracks for the 13 floats that cycled only through the left plume are shown in the upper panel of Fig. 8, while floats that went only through the right plume are shown in the lower panel. There is a distinct difference in the character of the float tracks for the two plumes and thus for the water parcels descending in the plumes. The floats associated with the left plume are injected more deeply into the tank while those of the right plume are more involved in the local, shallow recirculation. This is consistent with the observation from Fig. 6 that it is primarily fluid that descends in the left plume that ventilates the deep water in the tank and that this process occurs in episodic sinking events interrupted by freshwater sweeping across the top of the tank.

The maximum horizontal velocity in the interior of the tank measured across a line 44 cm from the left wall is shown in Fig. 9. The numerical model evolves interior

velocities in a way similar to that observed in PR1 but with more variability. The initial velocity, about 0.8 cm s^{-1} , is close to the observed value there (0.7 cm s^{-1}). The spin up of the tank is fully resolved in time by the numerical model, and it can be seen that the maximum value is reached in about 2 minutes. The numerical model comes to its equilibrium velocity in a shorter time than the laboratory experiment: somewhat over 10 minutes versus 30 minutes. This timescale is set by the time it takes the signal from the fresh source to propagate along the top of the box and interact with the dense plume, decreasing the buoyancy flux into the interior of the tank. The box is shorter in the numerical experiment than the laboratory experiment (0.75 m versus 0.92 m), but not enough to explain all of the discrepancy. Part of the difference is due to the fact that in the laboratory experiment the surface buoyancy sources were approximately point sources, while the numerical sources are line sources; in the laboratory the freshened surface wa-

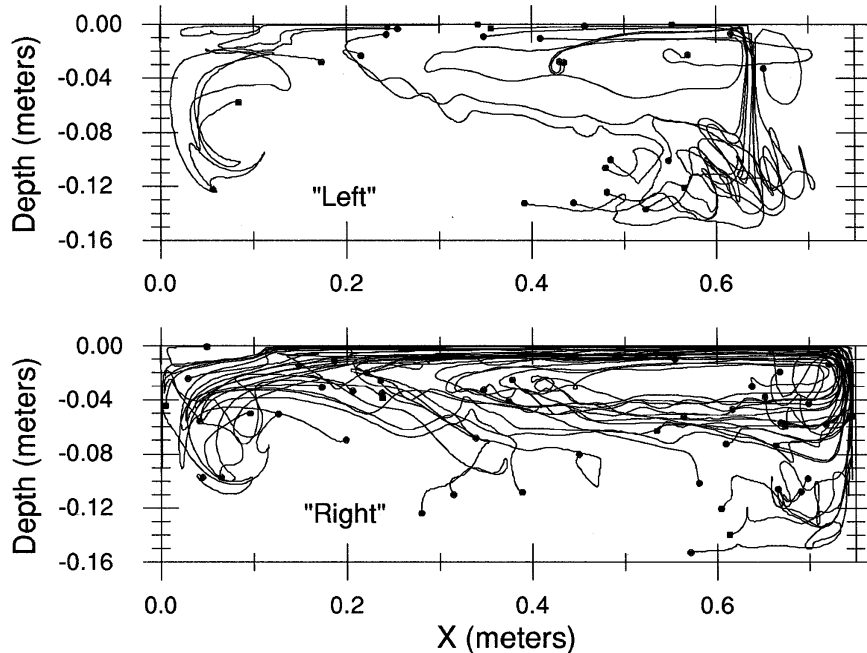


FIG. 8. Tracks of floats in the left and right plumes.

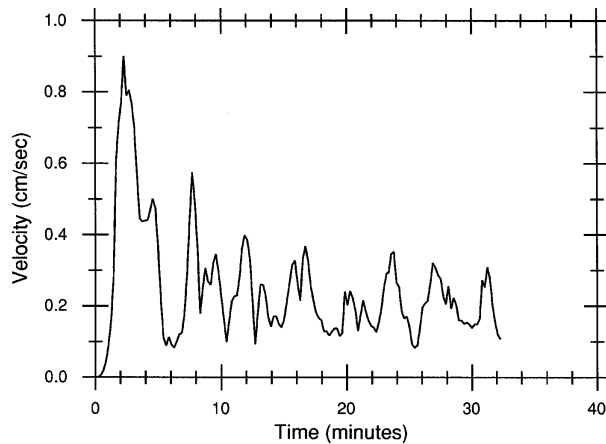


FIG. 9. Time evolution of the maximum interior velocity for the control run.

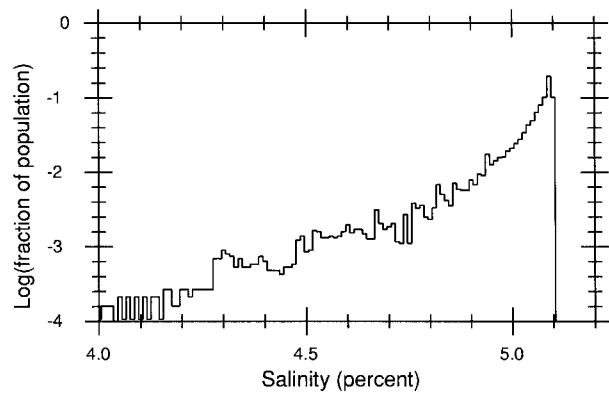


FIG. 10. Distribution of salinities in the control run after 35 min. Bins are 0.01% wide; the log of the fraction of population in the bin is plotted on the y axis.

ter was obliged to spread outward before propagating along the surface. Additionally, sidewall friction is present in the laboratory but not in the numerical model; this will tend to retard the surface plume's flow in the laboratory. (Note that endwall and bottom friction are included in the numerical model.)

The population distribution of salinities for the control run after 35 minutes is shown in Fig. 10. A pronounced asymmetry is clearly evident, with a large amount of water slightly saltier (and thus denser) than the initial value of 5% and a small amount of very light, fresh water. The asymmetry is caused by the tendency of the dense water to advect away from the densening source, preventing further densification, while the light water tends to remain near the freshening source, becoming increasingly fresh. The forcing conditions are a balanced flux dipole so the volume-averaged salinity in the tank must remain constant; however, the most common salinity does not have to remain at the initial value of 5%, and has increased.

The asymmetric salinity population in the model is similar to the highly skewed temperature distribution that occurs in the real oceans, shown in Fig. 11. Salinity in the numerical model is analogous to temperature in the ocean because the sense of the thermohaline circulation in the present epoch is determined primarily by temperature rather than salinity differences—thus, the close correspondence of model salinities (Fig. 10) to oceanic temperatures (lower panel of Fig. 11). By contrast, oceanic salinities less than 37.50 psu show no evidence on the large scale that densified water advects rapidly away from the densifying region; in fact, the distribution is roughly symmetric about the central peaks. It is interesting to note, however, that waters of salinity greater than 37.50 psu *do* have the characteristically skewed shape associated with a salinity-driven circulation. These are the Mediterranean Sea waters.

ENERGY EVOLUTION

The bulk energetics of the 2D model illustrate an interesting aspect of the potential energy balance. Assume that the working fluid has a linear equation of state and that exactly equal but opposite heat fluxes are being used to drive the system: Q watts of heating are applied at the surface at one end of the tank and Q watts of cooling at the other end. The applied heating produces

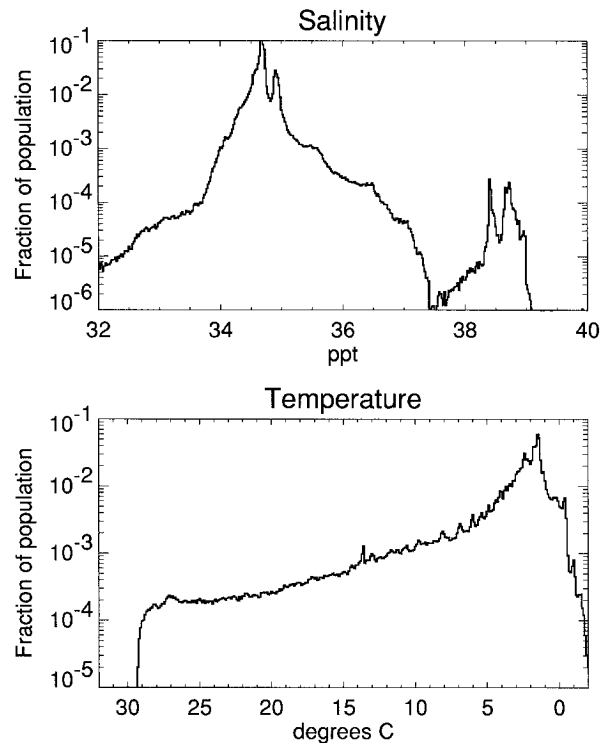


FIG. 11. Population distribution for ocean salinity (top) and temperature (bottom) based on annually averaged data from Levitus (1982). Both figures are plotted such that density increases to the right. Salinity bins are 0.02 psu wide; temperature bins are 0.1°C wide.

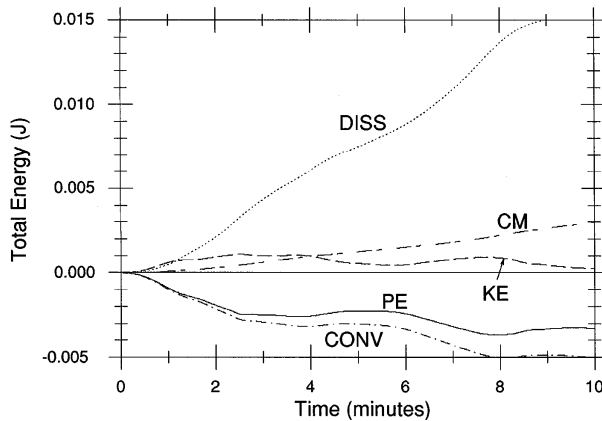


FIG. 12. Evolution of energies in the control run over the first 10 min. KE is the kinetic energy, PE is the potential energy, CONV is the KE to PE conversion term, DISS is the dissipation, and CM is the “center of mass” term. The latter three are time integrated.

a density change of $-\Delta\rho$, while the applied cooling produces a density change of $+\Delta\rho$. The heating and cooling are both applied on the same geopotential surface at height H . The total tank-integrated change in potential energy of the system due to all sources is then $(-\Delta\rho gH) + (+\Delta\rho gH) \equiv 0$. Thus, the sources do not directly change the volume-integrated potential energy of the system. Nevertheless, motions appear in the working fluid; this is because the initially homogeneous body of water has available potential energy to convert to kinetic energy. A heavy parcel injected at the surface will descend through the water column, releasing some of this PE; a light parcel injected at the surface, by contrast, cannot rise any farther. The result is that during the first few minutes a stratification is established, the center of mass of the system lowers, and this released potential energy is converted to kinetic energy.

Figure 12 shows the time evolution of the potential, kinetic, conversion, dissipation, and center of mass energies in the model [using the terminology from Eq. (3)] during the first 10 minutes. As discussed above, the potential energy drops rapidly when the experiment is initiated, while the kinetic energy increases. After about 5 minutes the initial heavy plume has moved along the bottom of the tank to the left-hand wall where it splashes up. This vertical advection of heavy water ($W\rho' > 0$) briefly increases the potential energy of the system at the expense of kinetic energy, the reverse of the typical conversion process.

The integrated dissipation term continues to increase as time goes on. This term is apparently unbalanced since the net tank-integrated input of potential energy by all the sources is identically zero, and kinetic energy cannot be extracted from the initial available potential energy indefinitely. This apparent imbalance is caused by the neglect of the pressure work term [PW in Eq. (3)], which is required to be identically zero in all models with an incompressible fluid despite the fact that

density changes are allowed. In actuality, the decrease in fluid density is accomplished by an expansion of fluid against pressure, thereby performing work on the surrounding fluid; the increase in density is accomplished by contraction with applied pressure, and work is performed by the surrounding fluid. In steady state, the constant dissipation is balanced by constant input of mechanical energy into the system through this (neglected) pressure work term. For this work to be positive, it follows that the expansion of the fluid must occur at a higher average pressure than the contraction. It should be noted that unbalanced dissipation is not a unique characteristic of this particular model; it will be a feature of *any* model that allows changes in density but also assumes incompressibility—which is to say, most oceanic GCMs.

The effect of rotation

The numerical model was configured as the zonal average of the three-dimensional equations of motion so that at least the rudimentary aspects of the rotating case could be examined. The rotation rate was chosen such that the Rossby number would be small, $U/fL \sim 0.01$. Using the values of U and L given in section 2, this gives a rotation rate of $f \sim 0.5 \text{ rad s}^{-1}$.

It is important to remember that the model is reentrant, with no side walls in the X direction; thus, there is no analog of “western boundaries” along which flow can develop. This configuration is similar to that studied in the laboratory by Hignett et al. (1981), who examined the long-term steady state of convection in a rotating annulus driven by a temperature gradient from below. They did not examine either the spinup of the system or (due to equipment limitations) the interior density structure. Both of these are amenable to examination with a numerical model.

Figure 13 shows the salinity field in the rotating model, 0.5 minutes after initiation of the experiment. The corresponding figure for the nonrotating case is also shown for comparison. In the presence of rotation the degree to which the nose of the plume can spread horizontally is restricted, as has been described by Jones and Marshall (1993). It can also be seen that the plume penetrates farther in the same amount of time.

The population distribution of salinity in the rotating model after 15 minutes is shown in Fig. 14. The range of salinities encountered in this case is far wider than in the control case. This is due to the rotational inhibition of overturning in the tank; fluid parcels spend a longer time near the forcing regions when the system is rotating. The boundary conditions are flux driven rather than set-value so that the longer parcels remain near the forcing spots, the more extreme value of salinity they will take on. As a result, both the maximum and minimum salinities are greater than in the control case.

The population peak near 5.3% grows with time during the 80 minutes the model was run. It arises from

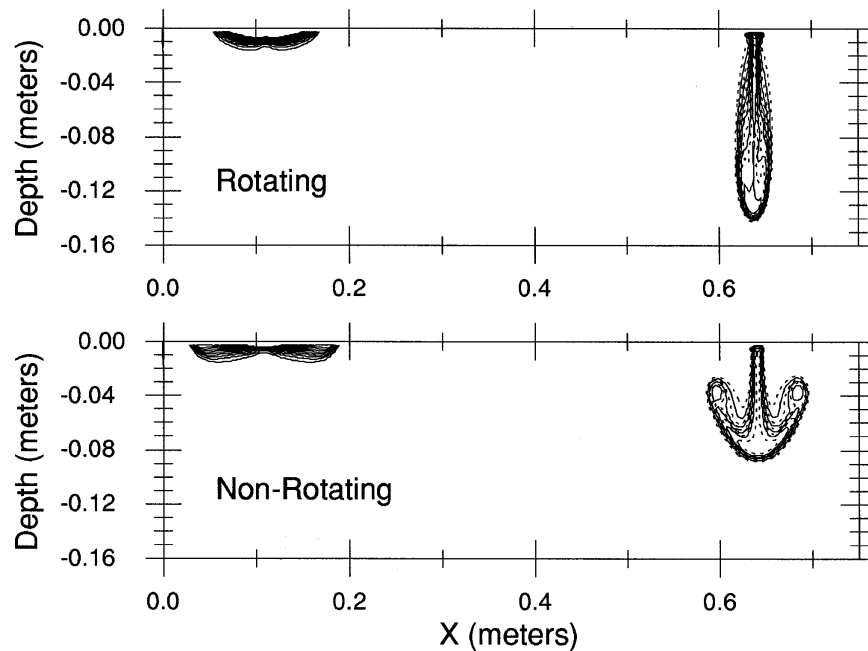


FIG. 13. Salinity field for the rotating test case (upper panel) after 0.5 min. The field for the nonrotating case (lower panel) is also shown for comparison.

mixing that the descending dense plume generates in the interior of the tank. This interior mixed region can be seen in Fig. 15, the salinity field after 80 minutes, underneath the dense plume between the 5.30% and 5.35% isohalines. Similar but smaller peaks that are remnants of individual dense plumes can be seen in Fig. 14 between salinities of 4.5% and 5.0%.

The hydrostatic case

It is instructive to compare the results shown above with the results of the model configured as a hydrostatic system. The motivation for doing this is that large-scale

models of the oceanic circulation use a similar set of equations to the ones used here but with the hydrostatic assumption made from the outset. Since the nonhydrostatic results are known in this case, comparing them with the results of a hydrostatic model should indicate specific ways in which hydrostatic models yield different simulation results than the case when fuller physics are included. A caveat that must be kept firmly in mind is the difference in scale of the nonhydrostatic plumes for a global 2D model versus the small-scale model used here. In a global 2D model the expected size of the nonhydrostatic convective plumes is far smaller than one grid point, while in the small-scale model the plumes are resolved by several grid points. Nevertheless, the comparison can yield some interesting insights into the difference in behavior between the two situations, and it should be remembered that even in the large-scale models the hydrostatic assumption is not valid in the convecting regions.

The hydrostatic model was constructed by changing the vertical momentum from a fully prognostic one in the vertical velocity w to a simple hydrostatic balance

$$p'_z = -g\rho'. \tag{4}$$

Along with this change to the equations, the treatment of the tracer fields was altered to prevent a statically unstable condition from persisting; that is, a “convective adjustment” scheme was added. The scheme used here is one common in large-scale oceanic modeling: under statically unstable conditions, the vertical diffusion constant between gridboxes is set to a value several orders of magnitude larger than the value used in stable

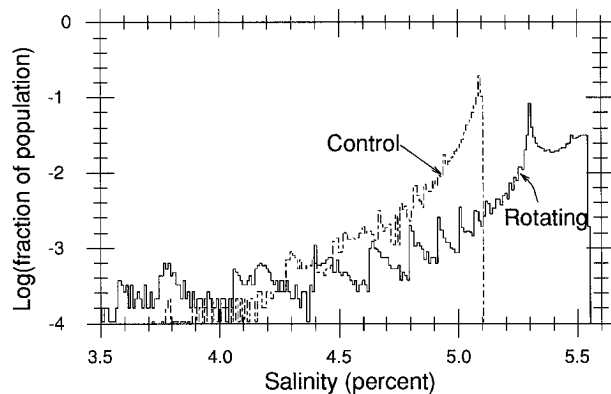


FIG. 14. Distribution of salinities in the rotating run after 15 min. Bins are 0.01 psu wide; the log of the fraction of population in the bin is plotted on the y axis. The data for the control run is shown for comparison.

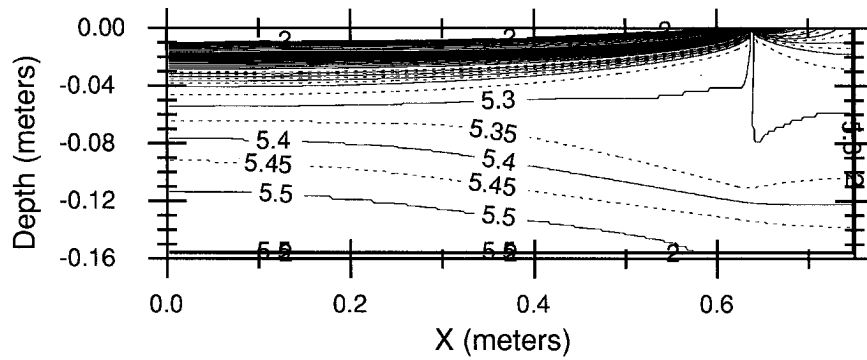


FIG. 15. Salinity field for the rotating case, 80 min.

conditions. The vertical diffusion equation is then solved implicitly to prevent instabilities. This scheme effectively removes the instability in just a few model time steps. This scheme was deliberately chosen to be similar to that used in large-scale modeling so that comparisons with such models would be more straightforward.

Figure 16 shows the salinity field for the hydrostatic run at time $T = 2$ min. This can be directly compared to the top panel of Fig. 3, the control model for the same time. There are a number of interesting differences between the model making the hydrostatic approximation and the control run. First, the hydrostatic model is noisier than the nonhydrostatic one. V. Sheremet (personal communication, 1992) has pointed out that hydrostatic models have a $2\Delta x$ gridpoint instability that arises in potentially statically unstable conditions. The instability is due to the removal of the vertical velocity information from the internal gravity wave equation, which then becomes unbounded in growth rate. Ordinarily this small $2\Delta x$ effect is easily damped out by horizontal viscosity, and test runs of this model with higher viscosities indeed showed that the noise could be similarly damped. The undamped runs have been used here both to be consistent with the control run and to emphasize the point that a properly constructed nonhydrostatic model can have *less* noise than the hydrostatic model at low viscosities. Another cause of this

noise is propagating pressure waves that generate weak vertical instabilities due to truncation errors in the advection algorithm. Convection rapidly mixes these with a large diffusion coefficient, while in the nonhydrostatic case the marginally heavy parcel falls quite slowly.

The second point is that the dense fluid in the hydrostatic run has penetrated farther into the fluid in the same amount of time compared to the control run. The behavior can be understood from Fig. 17, which shows the salinity fields in the hydrostatic (upper panel) and control model (lower panel) at 0.25 minutes. At this time the control model has just begun to form the dense plume that ultimately descends from the source, drawing salty fluid to the bottom of the tank. The situation with the hydrostatic model is quite different; the statically unstable conditions underneath the dense source force a persistent column of convectively adjusted water immediately below, which rapidly averages the high salinity values over the depth of the water column. Once this convecting column is initiated, its high diffusivity makes it function as a kind of “pipeline” whereby surface conditions are injected directly into the deep fluid. The dense plume moves away from this source region without having had to fall vertically through the tank, which is why it has advanced farther than the plume in the control case (Fig. 16).

The third manner in which the hydrostatic case differs appreciably from the control is in the structure of the

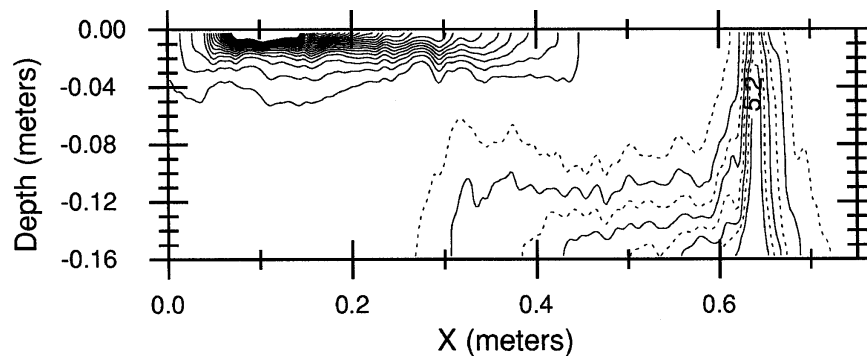


FIG. 16. Hydrostatic test case, $T = 2$ min.

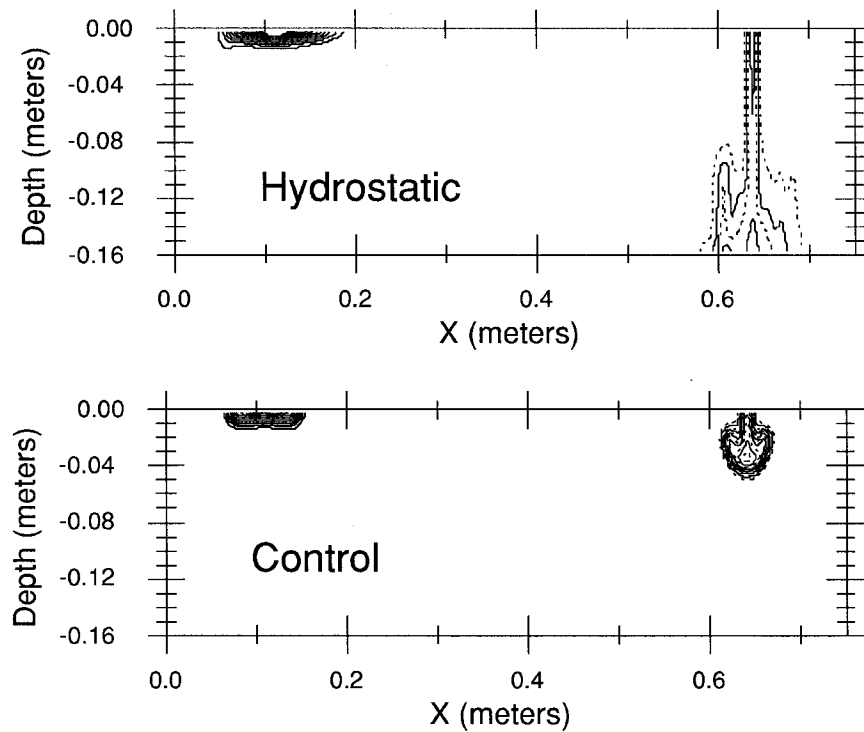


FIG. 17. Contours of salinity after 0.25 min for the hydrostatic test case (upper panel) and the control case (lower panel).

“nose” of the dense plume that propagates along the bottom of the tank. The hydrostatic model cannot support the kind of density inversion that is evident in Fig. 3, and the dense water sinks into the body of the plume. The feature is thus spread out over a larger vertical extent than is seen in the control model.

The average salinity field in the hydrostatic model after 35 minutes is shown in Fig. 18. The differences from the control case (Fig. 4) are interesting. The control case goes through the previously described four-stage cycle; the hydrostatic model does not exhibit such an oscillation. The hydrostatic model has a pycnocline that is approximately twice as thick as the nonhydrostatic model; this is evocative of the overly thick thermoclines

commonly found in primitive equation OGCMs, which generally make the hydrostatic assumption. This thicker pycnocline is due to the same processes that cause greater noise and enhanced mixing in the hydrostatic model, that is, the gridpoint instability and convective mixing triggered by truncation errors, as described above. In a model that uses a centered-differencing advection algorithm, overshoots and other nonmonotonic behavior could generate similar extraneous convective mixing.

In the hydrostatic model the entire portion of the tank to the right of the dense source has been vertically homogenized by contact with the dense source. Freshwater from the light source is incapable of advecting past the dense source, as happens with regularity in the four-

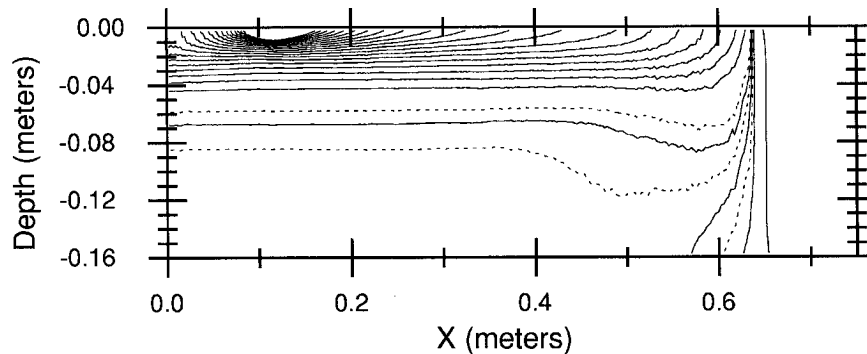


FIG. 18. Average salinity field after 35 min for the hydrostatic test case.

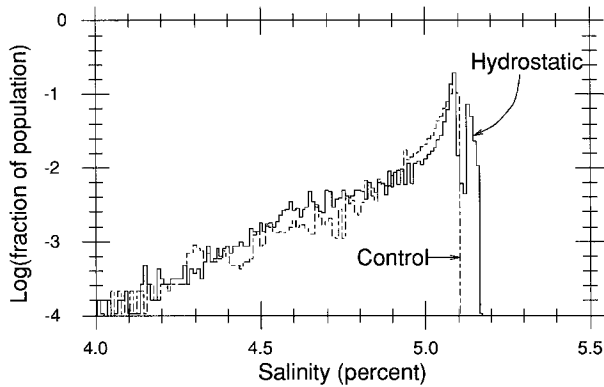


FIG. 19. Population distribution of salinity for the hydrostatic model at 35 min. The control run is shown for comparison.

stage cycle of the control run. Instead, the convective column forms a barrier to the flow. Water to the right of this barrier is almost isolated from the fresh source; as a result it is distinctly saltier than the interior fluid, as can be seen in the population distribution of salinities after 35 minutes (Fig. 19). An additional peak in the distribution for the hydrostatic case can be seen at a salinity of about 5.13%. Thus, there is a systematic difference in evolved salinities between the hydrostatic and nonhydrostatic models. This difference, however, could be ameliorated by three-dimensional flow around the convective source. Whether such a flow would be possible in a particular case depends on the details of the topography, surface forcing, etc.

The circulation that the hydrostatic model develops is also different from the control case. The average streamfunction after 35 minutes is shown in Fig. 20. Note that the contour interval is twice that used in the control run (Fig. 5). The flow is stronger than in the control case and has more deep flow. Upwelling through the halocline is more broadly distributed with much of the flow apparently avoiding the fresh region altogether, unlike the control case.

High-diffusion test case

The effect of anomalously high diffusion (either numerical or explicit) on the results of numerical models

is another area of interest. To explore the effect that anomalously high diffusion (either numerical or explicit) has on the results shown here, a series of runs was performed with both viscosity and diffusivity set to $5 \times 10^{-6} \text{ cm}^2 \text{ s}^{-1}$, five times higher than the control value.

Figure 21 shows the salinity field for the high-diffusion run at $T = 2$ min. The figure can be directly compared to the top panel of Fig. 3, the field for the control case at the same time (and plotted with the same contour intervals). The high-diffusion run shows a number of differences that are not surprising: the fields are generally more diffuse and have advanced farther than in the control case. The salinity values at the nose of the advancing plume are the same as those in the control case, but the dense fluid behind the nose has advanced farther. The outline of the eddy above and behind the nose of the advancing dense plume can be seen but has been eroded by diffusion and so lost its definition and decreased in amplitude.

It is more interesting to observe what has happened to the four-state cycle that was illustrated in Fig. 6 for the control case. A similar set of pictures for the high-diffusion test case is shown in Fig. 22. In the high-diffusion run the dense plume never detaches from the end wall. Dense fluid thus reaches the interior via a boundary layer rather than being injected directly into the interior of the fluid, as was the case with the control run. In the control case, dense water periodically detached from the dense source and was injected into the tank just below. In the high-diffusion case, this is now the site where *light* fluid is engulfed by a persistent eddy formed by the “sloshing” of water back and forth in the tank. The sloshing behavior proceeds despite the higher value of the diffusion and has the distinct effect of modulating the amount of dense water that penetrates to the interior of the tank. This is not as strong as in the control case, where the water column actually gets capped off and the dense plume ceases due to periodic surges of freshwater, but the remnants of this behavior can be seen in the variability of the dense plume’s transport.

The average salinity field after 20 minutes is shown in Fig. 23. The bowl shape of the halocline is more

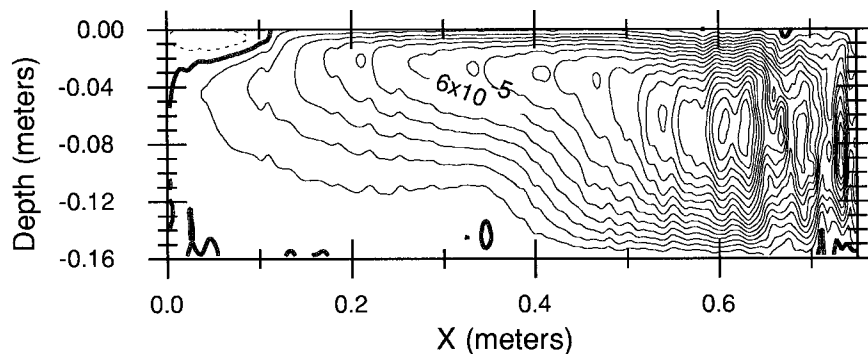


FIG. 20. The average streamfunction field for the hydrostatic test case after 35 min.

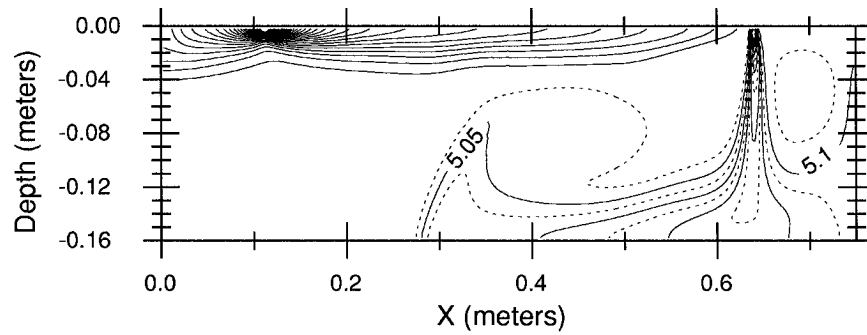


FIG. 21. Contours of salinity for the test run with diffusion 5 times that of the control run. $T = 2$ min.

evident than in the control run and the ventilation path of the model's deep water is specifically evident as a narrow umbilical running from the dense source to the wall and thence to the deep interior. Even in this high-diffusion case, however, the halocline is not as thick as the hydrostatic case.

The average streamfunction field after 20 minutes is shown in Fig. 24. The observation from the salinity

fields that the flow never detaches from the right-hand wall is borne out; there is no indication of descent underneath the dense plume. Additionally, the flow ventilates the bottom of the tank in a smoother and more constant fashion than in the control model. In fact, the streamfunction is more similar to the hydrostatic case than to the control case, which is consistent with the idea that the addition of the convective algorithm greatly increases the overall mixing in the tank.

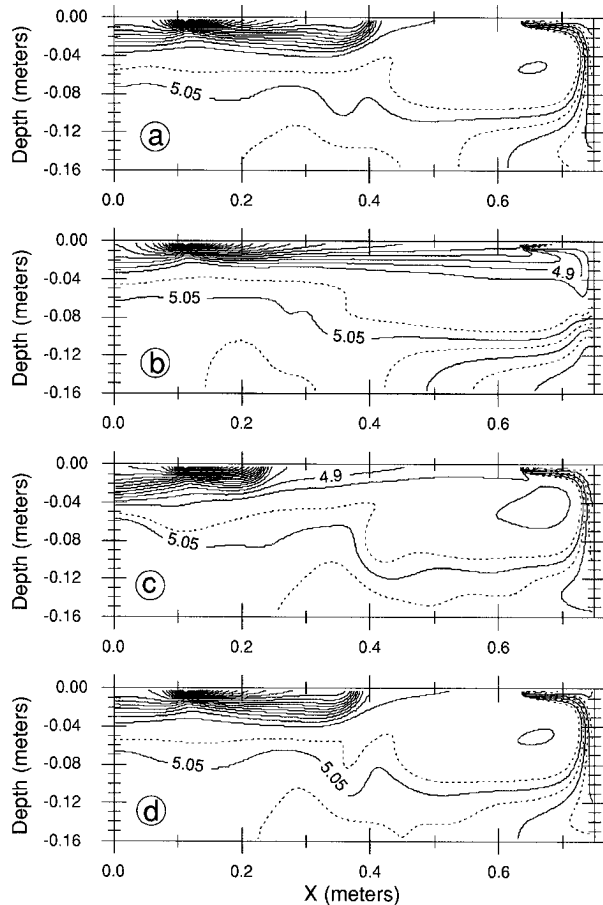


FIG. 22. High-diffusion test case, illustrating the high-diffusion analog to the control run's intermittent "deep water" renewal.

4. Discussion

It is interesting to compare the circulation evolved by the hydrostatic model to the nonhydrostatic control model. The primary circulation in the control model (Fig. 5) penetrates no deeper than halfway into the tank, while in the hydrostatic case (Fig. 20) it is close to symmetric about the center of the tank, just as observed in PR1. This is despite the fact that the hydrostatic model includes highly simplified physics to handle the convective adjustment.

The primary reason for this can be understood by recalling from PR1 the behavior of the laboratory experiment when a sloping bottom was inserted underneath the dense source. In that case the dense plume lifted off the bottom of the tank and circulation was mostly at intermediate depths, just as in the control case here. This happened in the laboratory case because reduced entrainment allowed the tank to fill from the bottom up, lifting the plume off the bottom once the influence of the surface light water on the dense plume was felt. In the laboratory experiment without a bottom slope the circulation never lifted off the bottom because the entrainment was too large.

There is analogous behavior in the two numerical models. The circulation in the control case lifts off the bottom of the tank, while the hydrostatic model's circulation remains essentially symmetric about middepth. The mixing (and therefore numerically simulated entrainment) is large in the hydrostatic case because of the algorithm used to implement the convective adjustment. It follows that the entrainment in the control case must be less than it should be for an accurate sim-

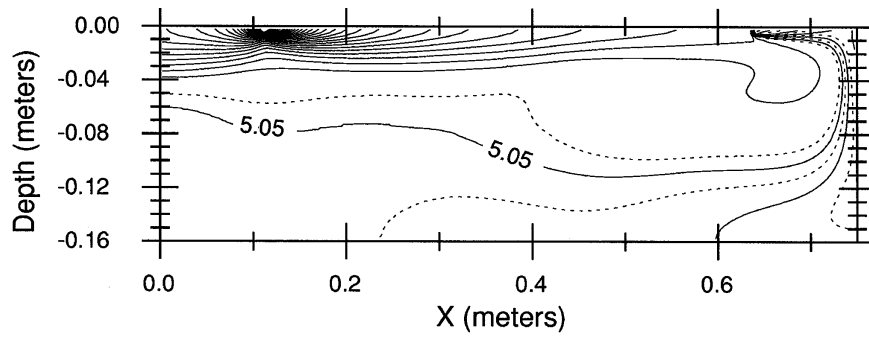


FIG. 23. The average salinity field after 20 min in the high-diffusion test case.

ulation, given the observation that the tank fills with dense water and the plume lifts off the bottom.

The difference in boundary conditions between the laboratory experiment and the numerical model might also be thought to have some effect. Recall that in PR1, the buoyancy flux is accomplished via small but finite volume fluxes; here there are no volume fluxes. This was examined in a test case where the fluid densities near the sources were set to the desired values, rather than changed via buoyancy fluxes. This simulates the instantaneous withdrawal and replacement of a small volume of fluid near the sources with fluid already at the target density. The result was that the four-stage cycle took approximately twice as long and was more irregular as well. Examination of this case showed that the surface freshwater flows and eddies were sometimes too weak to cap off the water column and prevent the dense plume from sinking. As a result, the time-averaged circulation pattern was a bit deeper than in the control case (Fig. 5), but far from being as symmetric as in the hydrostatic case (Fig. 20). Thus, the difference in boundary conditions between the laboratory and numerical cases has an influence toward encouraging the numerical case's plume to lift farther from the bottom of the tank, but the difference in entrainment is the stronger effect.

The hydrostatic model overestimates mixing in the region between the dense source and the right-hand wall (Fig. 18). It is virtually impossible to have horizontal surface flow past the dense source because the high

diffusivities associated with the convective adjustment scheme distribute the freshwater signature over the entire water column, with the result that no coherent signal is ever seen to the right of the dense source. Salinities in this region are therefore quite poorly represented. However, three-dimensional flow, not allowed in the two-dimensional model used here, might reduce this effect.

More illumination is shed on the difference between the hydrostatic and nonhydrostatic results by considering the results of the high-diffusion model. The streamfunction in this case (Fig. 24) shows that flow is continuously penetrating to the bottom of the water column just as in the laboratory experiment and in the hydrostatic model. This is consistent with the view that the control model's plume lifts off the bottom of the tank due to insufficient entrainment, which is made up for by greater overall diffusion in the high-diffusion test case. However, the high-diffusion model achieves this by trapping the flow to the right-hand wall; dense fluid only enters the deep part of the tank via this boundary current. This is quite different from the flow observed in the laboratory experiments of PR1 although it is reminiscent of the flow observed by Rossby (1965) in his laboratory experiments, which were performed with a linear gradient of forcing and generally at high viscosities.

These results support the idea that it is critical to correctly model the overall entrainment and detrainment in convective regions to accurately simulate buoyancy-

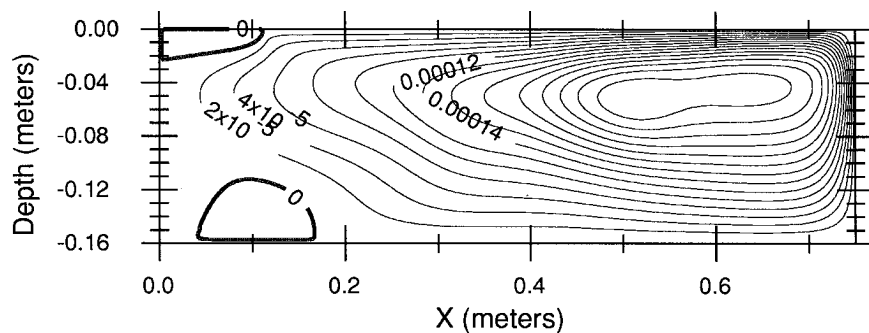


FIG. 24. The average streamfunction field after 20 min in the high-diffusion test case.

driven, meridionally overturning flows such as the earth's thermohaline circulation. Much of the deep structure in the flows modeled here was directly set by the overall entrainment and detrainment patterns in the convective region. In the laboratory experiments of PR1 it was additionally shown that the time-dependent behavior of the deep ventilation is sensitive to the overall entrainment. The time variability seen here is mostly a result of a repetitive cycle of motions that involves freshwater capping off the dense source and a dense plume subsequently punching through the cap. This cycle is damped as the mixing is increased and disappears entirely when the hydrostatic assumption and a convective adjustment scheme that has high mixing are added. This suggests that large-scale models that employ a convective adjustment scheme, or otherwise have unrealistically high values of mixing, may damp some natural variability associated with this process.

5. Conclusions

We have examined the process of building a pycnocline by using a two-dimensional, nonhydrostatic model configured to be similar to the laboratory experiments of Pierce and Rhines (1996); the forcing is a balanced dipole of salinity fluxes with a net density change of zero. This methodology allows us to examine aspects of the laboratory system that are difficult to measure without disturbing the flow, such as the overall energetics and the population distribution of densities. Our conclusions are as follows.

- 1) The control case's analog of deep-water ventilation occurs intermittently despite the constant surface forcing. The ventilation is accomplished through a repetitive cycle: (i) Freshwater propagates along the top of the tank from the freshening to the densifying source. (ii) The freshwater caps off the water column under the dense source, preventing ventilation of the deep waters. (iii) The freshwater under the densifying source gradually increases in density until it punches through the halocline and initiates deep ventilation. The cycle then repeats.
- 2) The tendency of light water to remain under the lightening source and dense water to rapidly convect away from the densifying source produces a characteristically skewed population distribution of density. With a balanced surface density flux, the mean density remains constant, but the most common density becomes considerably denser than the mean. This skewed population density can be seen in the World Ocean's temperature distribution but not in the salinity distribution, which is consistent with the fact that the earth's thermohaline circulation is thermally direct. The Mediterranean Sea waters are an exception to this; they show a distribution consistent with a saline-direct large-scale circulation.
- 3) The presence of rotation has a strong impact on the

evolved density distributions. Rotation inhibits meridional flow with the result that water remains near the sources for a longer time. As a result, the rotating system shows a considerably wider range of densities than the nonrotating system.

- 4) There were significant differences between the behavior of the nonhydrostatic control case and a test case that used the hydrostatic assumption and a convective adjustment scheme. The hydrostatic case evolved noisier fields than the fully nonhydrostatic model due to the enhanced mixing; also, the range of salinities evolved by the hydrostatic model was larger than in the the control model since part of the tank was isolated by a strong convective barrier to flow.
- 5) Although the balanced sources do not directly cause any change in the volume-integrated potential energy of the system, motions appear in the fluid because the initially homogeneous body of water has available potential energy that can be tapped. After the available potential energy is released, motions continue (and energy is internally dissipated) although no energy is apparently being supplied to the system. This is because the pressure work term is neglected in the model used here and in most oceanic general circulation models, which specify an incompressible fluid despite allowing changes in density.

Acknowledgments. We would like to thank an anonymous reviewer for pointing out the effect that the difference in boundary conditions might have on the experiment, as described in section 4.

APPENDIX

Derivation of the Model Equations

a. Momentum equations

The model derivation begins with the decomposition of the pressure and density fields into horizontally averaged and perturbation components

$$\rho = \bar{\rho}(z, t) + \rho'(x, y, z, t) \approx \rho_o \quad (\text{A1})$$

$$p = \bar{p}(z, t) + p'(x, y, z, t). \quad (\text{A2})$$

Consistent with the Boussinesq assumption, it is assumed that a characteristic density for the system ρ_o can be sensibly chosen and used in terms other than the buoyancy forcing. The background hydrostatic state is simply $\bar{p}_z = g\bar{\rho}$.

After subtracting off the background hydrostatic state, the momentum equations become

$$\frac{Du}{Dt} - fv + hw = -\frac{p'_x}{\rho_o} + \nu\nabla^2u \quad (\text{A3})$$

$$\frac{Dv}{Dt} + fu = -\frac{p'_y}{\rho_o} + \nu\nabla^2v \quad (\text{A4})$$

$$\frac{Dw}{Dt} - hu = -\frac{p'_z}{\rho_o} - \frac{g}{\rho_o}\rho' + \nu\nabla^2w, \quad (\text{A5})$$

where u , v , and w are the velocity components, $f = 2\Omega \sin\theta$, $h = 2\Omega \cos\theta$, Ω is the rotation rate of the earth, θ is the latitude, ν is viscosity, ρ' is the perturbation density, and ρ' is the perturbation pressure.

The horizontal Coriolis terms in Eqs. (A3) and (A5) cannot be generally neglected in nonhydrostatic cases since the vertical velocities and accelerations can be large. However, this model's purpose is to supplement laboratory experiments where the rotation vector will always be aligned with the vertical. In such cases $\cos\theta \equiv 0$, and the horizontal Coriolis terms do not appear.

The density equations for the system are

$$\frac{D\theta}{Dt} = \kappa_\theta\nabla^2\theta \quad (\text{A6})$$

$$\frac{DS}{Dt} = \kappa_S\nabla^2\theta \quad (\text{A7})$$

$$\rho = \rho(\theta, S), \quad (\text{A8})$$

where θ is the potential temperature, S is the salinity, and the applicable diffusivities are κ_θ and κ_S . In most of the experiments shown here, either temperature or salinity (but not both) was used.

The fluid is assumed to be incompressible;

$$\nabla \cdot \mathbf{u} = 0. \quad (\text{A9})$$

The nonhydrostatic system of equations using this assumption is typically called the "anaelastic" system and was first studied in this context by Ogura and Phillips (1962).

A two-dimensional model is constructed by taking the horizontal average of the equations given above and assuming periodicity in X . A similar approach was taken by Smith (1989). Letting the horizontal averaging operator be indicated by angle brackets,

$$\langle * \rangle = \frac{1}{2L} \int_{-L}^L * dx, \quad (\text{A10})$$

and letting capital letters indicate horizontally averaged quantities (so $U = \langle u \rangle$, $P = \langle p' \rangle$, etc.), the momentum and mass continuity equations become

$$\frac{\partial U}{\partial t} + \langle vw_y + wu_z \rangle - fV = \nu\nabla^2U \quad (\text{A11})$$

$$\frac{\partial V}{\partial t} + \langle vw_y + wu_z \rangle + fU = -\frac{P_y}{\rho_o} + \nu\nabla^2V \quad (\text{A12})$$

$$\frac{\partial W}{\partial t} + \langle vw_y + wu_z \rangle = -\frac{P_z}{\rho_o} - \frac{g}{\rho_o}\rho' + \nu\nabla^2W \quad (\text{A13})$$

$$V_y + W_z = 0, \quad (\text{A14})$$

where the terms with x derivatives have vanished due to the periodic boundary conditions in x . The mass continuity equation then suggests defining a streamfunction:

$$\Psi_z = -V \quad (\text{A15})$$

$$\Psi_y = W. \quad (\text{A16})$$

This simplifies the solution procedure since an impermeable boundary can easily be implemented by setting Ψ constant on the boundary.

The pressure can be eliminated by forming a horizontal vorticity equation from the curl of the V and W momentum equations:

$$\frac{\partial \zeta}{\partial t} + U \cdot \nabla \zeta - (fU)_z = -\frac{g}{\rho_o}\rho'_y + \nu\nabla^2\zeta, \quad (\text{A17})$$

where $\zeta = W_y - V_z \equiv \nabla^2\Psi$. The Coriolis parameter f is taken to be constant. In this step we assume that averages of products are the same as products of the averages, that is, that $\langle vw_y \rangle = \langle v \rangle \langle w_y \rangle = VW_y$, etc. Since the averaging is being performed in the x direction, this assumption removes the role of eddy transports in that direction. This 2D model has no extent in the x direction, however, so the omission is not a drawback. Eddy transports in the y - z plane can still be developed.

The previous assumption also allows us to write the U momentum equation as

$$\frac{\partial U}{\partial t} + VU_y + WU_z - fV = \nu\nabla^2U. \quad (\text{A18})$$

Finally, using the definition of Ψ , Eq. (A17) becomes

$$\frac{\partial}{\partial t}\nabla^2\Psi + J(\Psi, \zeta) - (fU)_z = -\frac{g}{\rho_o}\rho'_y + \nu\nabla^2\zeta, \quad (\text{A19})$$

which is Eq. (1).

b. Energy equations

An equation for the kinetic energy of the system \mathcal{K} can be obtained by multiplying Eq. (A11) by U , Eq. (A12) by V , Eq. (A13) by W , and summing:

$$\begin{aligned} \frac{D\mathcal{K}}{Dt} &= -\tilde{U} \cdot \nabla P - Wg\rho' + \nu\nabla^2\mathcal{K} - \rho_o\epsilon \\ &= \nabla \cdot (-P\tilde{U} + \rho_o\nu\nabla\mathcal{K}) - Wg\rho' - \rho_o\epsilon \\ &\quad + P\nabla \cdot \tilde{U}, \end{aligned} \quad (\text{A20})$$

where $\mathcal{K} \equiv (\frac{1}{2})\rho_o(U^2 + V^2 + W^2)$, $\tilde{U} \equiv (U\mathbf{i} + V\mathbf{j} + W\mathbf{k})$, and ϵ is the dissipation, defined by $\epsilon \equiv \nu((\partial\tilde{U}/\partial y)^2 + (\partial\tilde{U}/\partial z)^2)$.

If the geopotential Φ is taken to be equal to gz , then the potential energy can be defined as $\mathcal{P} \equiv \rho\Phi$. The evolution of the potential energy can then be written as

$$\begin{aligned}
\frac{D\mathcal{P}}{Dt} &= \rho \frac{D\Phi}{Dt} + \Phi \frac{D\rho}{Dt} \\
&= Wg\bar{\rho} + Wg\rho' + \kappa\nabla^2\mathcal{P} - 2\kappa g\rho_z + \Phi Q \\
&= \nabla \cdot (\kappa \nabla \mathcal{P}) + Wg\bar{\rho} + Wg\rho' - 2\kappa g\rho_z + \Phi Q.
\end{aligned}
\tag{A21}$$

Comparing Eqs. (A20) and (A21) shows that the $Wg\rho'$ term accomplishes the conversion from potential energy to kinetic energy.

The fourth term on the right-hand side of Eq. (A21) comes from the diffusion term and represents the change in potential energy of a system in a gravity field whose center of mass moves owing to diffusion.

If we are interested in the energy budget of a closed system, then Eqs. (A20) and (A21) can be integrated over the volume of the tank. The divergence terms on the right-hand side integrate to zero; the $Wg\bar{\rho}$ term in Eq. (A21) does also since $\bar{\rho}$ is constant over the width of the tank while W must integrate to zero over the width. We are left with Eqs. (2) and (3).

REFERENCES

- Colella, P., and P. R. Woodward, 1984: The piecewise parabolic method (PPM) for gas-dynamical simulations. *J. Comput. Phys.*, **54**, 174–201.
- Hignett, P., A. Ibbetson, and P. D. Killworth, 1981: On routing thermal convection driven by non-uniform heating from below. *J. Fluid Mech.*, **109**, 161–187.
- Jones, H., and J. Marshall, 1993: Convection with rotation in a neutral ocean: A study of open-ocean deep convection. *J. Phys. Oceanogr.*, **23**, 1009–1039.
- Levitus, S., 1982: *Climatological Atlas of the World Ocean*. NOAA Prof. Paper No. 13, U.S. Govt. Printing Office, 173 pp.
- Marotzke, J., and J. Willebrand, 1991: Multiple equilibria of the global thermohaline circulation. *J. Phys. Oceanogr.*, **21**, 1372–1385.
- Ogura, Y., and N. A. Phillips, 1962: Scale analysis of deep and shallow convection in the atmosphere. *J. Atmos. Sci.*, **19**, 173–179.
- Pierce, D. W., and P. B. Rhines, 1996: Convective building of a pycnocline: Laboratory experiments. *J. Phys. Oceanogr.*, **26**, 176–190.
- Rosby, H. T., 1965: On thermal convection driven by non-uniform heating from below: An experimental study. *Deep-Sea Res.*, **12**, 9–16.
- Smith, N. R., 1989: The Southern Ocean thermohaline circulation: A numerical model sensitivity study. *J. Phys. Oceanogr.*, **19**, 713–726.
- Smolarkiewicz, P. K., 1983: A simple positive definite advection scheme with small implicit diffusion. *Mon. Wea. Rev.*, **111**, 479–486.
- Stocker, T. F., D. G. Wright, and W. S. Broecker, 1992: The influence of high-latitude surface forcing on the global thermohaline circulation. *Paleoceanography*, **7**, 529–542.
- Winton, M., and E. S. Sarachik, 1993: Thermohaline oscillations induced by strong steady salinity forcing of ocean general circulation models. *J. Phys. Oceanogr.*, **23**, 1389–1410.